

Spin Hall conductivity in topological Dirac semimetals

Katsuhsia Taguchi¹, Daisuke Oshima², Yusuke Yamaguchi², Tatsuki Hashimoto¹, Yukio Tanaka², Masatoshi Sato¹

¹ *Yukawa Institute for Theoretical Physics, Kyoto University, Kyoto 606-8502, Japan*

² *Department of Applied Physics, Nagoya University, Nagoya 464-8603, Japan*

(Dated: March 4, 2020)

We theoretically investigate the spin Hall conductivity (SHC) in topological Dirac semimetals (TDSMs) whose Dirac points are protected by rotational symmetry. On the basis of a general phase diagram of the system with time-reversal, inversion and four-fold rotational symmetries, we reveal that the SHC is sensitive to the phase to which the system belong. The phase and the SHC are characterized by the mirror Chern numbers and the presence or absence of gapless bulk Dirac points. It is also found that the representative TDSM Cd_3As_2 supports a large and negative SHC $\sigma_{xy}^z \sim -10^4 (\hbar/e)(\Omega\cdot\text{m})^{-1}$. The principle behind the dependency of SHC on the phase diagram is also explained.

I. INTRODUCTION

Topological Dirac semimetals (TDSMs) are 3D materials having both a linear dispersion along all momentum directions and a nonzero topological invariant. Their Dirac points (DPs)(gapless points) are protected by rotational symmetry, and they exist stably along the rotational symmetric axis in a finite parameter region unlike an accidental Dirac semimetal existing at the topological phase transition point between a 3D topological insulator and a normal insulator¹. TDSMs can be distinguished from ordinary Dirac semimetals (DSMs) by the mirror Chern numbers $n_{\mathcal{M}}$ at $k_z = 0$ and π plane; $n_{\mathcal{M}} = 0$ in DSMs but $n_{\mathcal{M}} \neq 0$ in TDSMs. To date, TDSMs with rotational symmetry have been synthesized and experimentally demonstrated²⁻⁶.

Several characteristic phenomena specific to TDSMs have been studied theoretically and experimentally²⁻⁸. Among them, the spin Hall effect, *i.e.* spin current generation via an applied electric field, is intriguing. The spin Hall effect is a central issue in spintronics, and the non-dissipative spin current has a possible application to energy-saving electronic devices^{9,10}.

Whereas the spin Hall conductivity (SHC) of TDSMs has been discussed in the low-energy model Hamiltonian,⁷ a full lattice description is necessary to capture the whole phase diagram of TDSMs:¹ A general 3D lattice Hamiltonian possesses multiple phases, such as TDSM, DSM, and weak topological (crystalline) insulators¹, which are not reproduced in the low-energy model. Moreover, the low-energy description is known to have a subtle ambiguity in transport phenomena^{11,12}.

In this paper, we evaluate the SHC systematically based on a lattice model with time-reversal, inversion and four-fold rotational symmetries. First, we consider the low-energy limit of the model Hamiltonian. We derive the SHC analytically, and find that the SHC is proportional to the distance between DPs along the rotational symmetric axis (Γ -Z axis). The low-energy Hamiltonian accidentally preserves the spin in the z -direction, from which the simple relation is obtained. Then, we evaluate the SHC by using the full lattice model. We reveal

that the SHC is sensitive to the phase to which the system belong. The phase and the SHC are characterized by the mirror Chern numbers and the presence or absence of gapless bulk Dirac points. We also find that the SHC obtained in the low-energy limit reproduces that in the lattice model only in a part of the TDSM phase. The principle behind the dependency of SHC on the phase diagram is explained. Furthermore, since the SHC is given by the quantized unit of electrical conductance and the distance between DPs, we estimate that the representative TDSM Cd_3As_2 supports a large and negative SHC $\sigma_{xy}^z \sim -10^4 (\hbar/e)(\Omega\cdot\text{m})^{-1}$.

This paper is organized as follows. In Sec.II, we introduce a general model Hamiltonian of TDSMs that supports time-reversal, inversion and four-fold rotational symmetries. We also review the phase diagram of the system. In Sec.III, we calculate the SHC using the Green's functions techniques in the clean limit. In Sec.III B, we derive the analytical formula for the SHC in the low-energy description near the Γ point. The mixing effects in the low-energy description is discussed in Sec.III C. We provide the result of the SHC for the full lattice Hamiltonian in Sec.III D. In Sec. IV, we compare the full lattice calculation with the low-energy description. We also identify the topological invariant that explains a jump of the SHC at $M/t_z = 1$. Finally, we estimate the SHC for a candidate material Cd_3As_2 .

II. MODEL

To calculate the SHC, we consider a general Hamiltonian for TDSMs having time-reversal, inversion, and four-fold rotational symmetries. Assuming that the Hamiltonian consists of orbitals with opposite parity under inversion, we obtain the minimal Hamiltonian as follows,^{1,13,14}

$$H(\mathbf{k}) = a_1(\mathbf{k})\sigma^x s^z + a_2(\mathbf{k})\sigma^y s^0 + a_3(\mathbf{k})\sigma^z s^0 + a_4(\mathbf{k})\sigma^x s^x + a_5(\mathbf{k})\sigma^x s^y, \quad (1)$$

where $a_{i=1,2,3,4,5}$ is a real function given by

$$a_1(\mathbf{k}) = \eta \sin k_x \quad (2)$$

$$a_2(\mathbf{k}) = -\eta \sin k_y \quad (3)$$

$$a_3(\mathbf{k}) = M - t_{xy}(\cos k_x + \cos k_y) - t_z \cos k_z. \quad (4)$$

$$a_4(\mathbf{k}) = (\beta + \gamma) \sin k_z (\cos k_y - \cos k_x) \quad (5)$$

$$a_5(\mathbf{k}) = -(\beta - \gamma) \sin k_z \sin k_y \sin k_x. \quad (6)$$

Here, η indicates the nearest neighbor hopping amplitudes in the xy plane; $\beta + \gamma$ represents the next nearest neighbor hopping amplitudes in the yz and zx planes; $\beta - \gamma$ indicates the hopping process along the body-diagonal direction of the cubic lattice; $\sigma^{i=x,y,z}$ and $s^{i=x,y,z}$ are Pauli matrices in the orbital and the spin spaces, respectively; M indicates the on-site potential difference between the orbitals; t_{xy} (t_z) denotes the difference in hopping amplitudes between different orbitals along the x and y directions (along z direction). The Hamiltonian describes the TDSM phase in Cd_3As_2 where the orbital and the spin are given by $|s, \uparrow, J_z = 1/2\rangle$, $|p_x + ip_y, \uparrow, J_z = 3/2\rangle$, $|s, \downarrow, J_z = -1/2\rangle$, and $|p_x - ip_y, \downarrow, J_z = -3/2\rangle$ (\uparrow and \downarrow represent the spin degrees of freedom).

The Hamiltonian hosts time-reversal, inversion, and four-fold rotational symmetries

$$\mathcal{T}H(\mathbf{k})\mathcal{T}^\dagger = H(-\mathbf{k}), \quad (7)$$

$$\mathcal{P}H(\mathbf{k})\mathcal{P}^\dagger = H(-\mathbf{k}), \quad (8)$$

$$\mathcal{C}_4 H(k_x, k_y, k_z) \mathcal{C}_4^\dagger = H(k_y, -k_x, k_z), \quad (9)$$

with $\mathcal{T} = i\sigma^0 s^y \mathcal{K}$, $\mathcal{P} = \sigma^z s^0$, and $\mathcal{C}_4 = e^{i(2\sigma^0 - \sigma^z)s^z\pi/4}$, respectively. Combining inversion and rotation symmetries, we also have mirror reflection symmetry

$$\mathcal{M}_{xy} H(k_x, k_y, k_z) \mathcal{M}_{xy}^\dagger = H(k_x, k_y, -k_z) \quad (10)$$

with $\mathcal{M}_{xy} = \mathcal{P}\mathcal{C}_4^2 = i\sigma^0 s^z$. The four-fold rotational symmetry prohibits the mixing between different orbitals at a rotation symmetric line, which makes it possible to obtain stable DPs. Because of the mirror reflection symmetry, we can introduce the mirror Chern numbers at $k_z = 0$ and $k_z = \pi$, respectively. Note that the mirror Chern numbers are well-defined even if DPs exist, as long as DPs are not on a mirror invariant plane.

Following Ref.1, we present the phase diagram of the model Hamiltonian in Fig.1. Each phase is characterized by the mirror Chern numbers and the presence or absence of DPs. For $M/t_z + 2t_{xy}/t_z - 1 < 0$ (DSM phase), DPs both at Γ - Z and M - A lines in the Brillouin zone [Fig. 1(c)], and the mirror Chern numbers are zero both at $k_z = 0$ and π . For $M/t_z \pm 2t_{xy}/t_z \mp 1 > 0$ and $M/t_z - 2t_{xy}/t_z - 1 < 0$ (TDSM phase), DPs are located only at a line between Γ and Z points, and the mirror Chern number is nonzero at $k_z = 0$ [Fig. 1(b),(e)]. Finally, in $M/t_z - 2t_{xy}/t_z + 1 < 0$ (weak topological insulator (WTI)/topological crystalline insulator (TCI) phase), the system is fully gaped in the bulk and has nonzero mirror Chern numbers [Fig. 1(a),(d)].

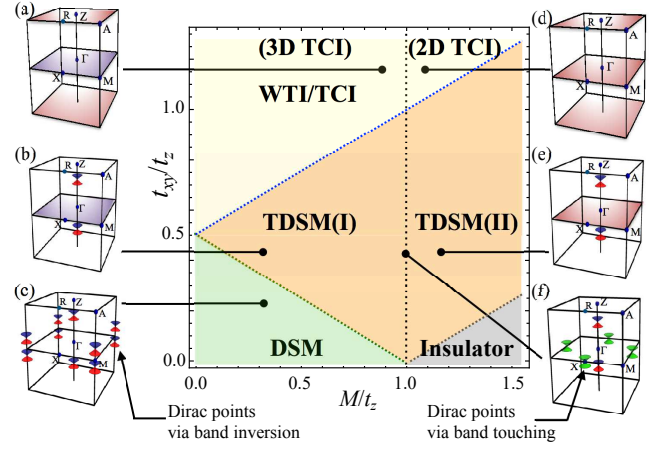


FIG. 1. (Color online) Phase diagram of the system, where M and t_{xy} (t_z) denotes the on-site potential difference between the orbitals and the difference in hopping amplitudes between different orbitals along the x and y directions (along z direction), respectively¹. The phases are characterized by the mirror Chern numbers and the presence or absence of DPs. (a)-(f) indicate the location of DPs via band inversion (represented by red and blue cones) and band touching (represented by green cones) in the Brillouin zone. Here, the band-touching DP are on the boundaries of the phases (dotted lines in the phases). At $\beta + \gamma = 0$, DPs exist even at the X -point in the $M/t_z < 1$ regime. The red (blue) plane in the Brillouin zone shows the nonzero mirror Chern number $n_M = +1(-1)$ at in $k_z = 0$ and π plane.

We notice that the mirror Chern number at $k_z = 0$ changes by a factor of two at $M/t_z = 1$ line in the TDSM and WTI/TCI phases. The change is caused by a band touched Dirac dispersion at the X point for $M/t_z = 1$ [Fig. 1(f)]. The difference in the mirror Chern number refines both the TDSM and WTI/TCI phases. In particular, the WTI/TCI phase is refined into a 3D TCI [Fig. 1(a)] and a 2D TCI [Fig. 1(d)], respectively. We denote the refined phases as TDSM(I)[Fig. 1(b)], TDSM(II)[Fig. 1(e)], 3D TCI[Fig. 1(a)], and 2D TCI[Fig. 1(d)], respectively.

In addition to DPs protected by rotation symmetry, the system may have accidental DPs. Such accidental DPs appear along the X - R line when $M/t_z < 1$ and $\beta + \gamma = 0$. On the X - R line, the energy of the system is given by $E(0, \pi, k_z) = \pm \sqrt{a_3^2(k_z) + a_4^2(k_z)}$, which is gapless when $k_z = \pm \arccos(M/t_z)$ and $\beta + \gamma = 0$. For a non-zero $\beta + \gamma$, a gap opens at the gapless point, but it stays narrow for small $\beta + \gamma$. As we show later, such a narrow gap may provide a substantial contribution to the SHC.

III. SPIN HALL CONDUCTIVITY

In this section, we show the SHC of the model Hamiltonian $H(\mathbf{k})$. First, using the standard technique of the Keldysh Green's functions, we provide that the SHC is

represented by the momentum integral of the spin Berry curvature and the Fermi distribution functions [Eq. (16)]. Second, we calculate the SHC using Eqs. (16)-(18) and two different descriptions of the model; the low-energy description near DPs, and the full lattice description. The SHC is obtained analytically in the low-energy description near DPs, and we find that the SHC is proportional to the distance between DPs if the mixing between DPs is taken into account. We also perform the numerical calculation of the SHC in the lattice description of the model, and evaluate the phase dependence of the SHC.

A. Spin Hall conductivity

Spin current density is defined by¹⁰

$$j_{s,i}^\alpha = \langle \psi^\dagger v_{s,i}^\alpha \psi \rangle, \quad (11)$$

where $v_{s,i}^\alpha = \{v_i, \frac{\hbar}{2} s^\alpha \sigma^0\}/2$ is the velocity operator of the spin current, $v_i = \partial H/(\hbar \partial k_i)$ is the velocity operator, and $\psi^\dagger = (\psi_{s,\uparrow}^\dagger, \psi_{p_x+ip_y,\uparrow}^\dagger, \psi_{s,\downarrow}^\dagger, \psi_{p_x-ip_y,\downarrow}^\dagger)$ denotes the creation operator for the model Hamiltonian $H(\mathbf{k})$ on the spin degrees of freedom and the orbital degrees of freedom. The superscript and the subscript of the spin current $j_{s,i}^\alpha$ indicate the polarization of spin and the direction of its flow, respectively.

The spin current in a linear response caused by an external electric field along the y direction ($E_{\text{ex},y}$) is given by

$$\sigma_{xy}^z \equiv j_{xy}^z / E_{\text{ex},y}. \quad (12)$$

The SHC can be represented by the standard technique of Green's functions as follows:^{10,15}

$$\sigma_{xy}^z = \frac{e\hbar}{\Omega} \sum_{\mathbf{k}, \omega} \text{tr} [v_{s,x}^z G(\mathbf{k}, \omega) v_y G(\mathbf{k}, \omega + \Omega)]_{\Omega \rightarrow 0}^<, \quad (13)$$

where e represents the elementary charge of electrons, and $\Omega (\rightarrow 0)$ represents the frequency of the applied electric field $E_{\text{ex},y}$. Here, $G(\mathbf{k}, \omega)$ denotes the Green's functions of $H(\mathbf{k})$, and the superscript "<" indicates the lesser component of the Green's function. The SHC σ_{xy}^z can be decomposed into two terms, i.e., $\sigma_{xy}^z = \sigma_{xy}^{z,\text{ra}} + \sigma_{xy}^{z,\text{aa}}$, where $\sigma_{xy}^{z,\text{ra}}$ and $\sigma_{xy}^{z,\text{aa}}$ are constructed by the products of the retarded and the advanced Green's functions, and by only the advanced Green's functions, respectively, as follows:

$$\sigma_{xy}^{z,\text{ra}} = e\hbar \sum_{\mathbf{k}, \omega} \frac{\partial f(\omega)}{\partial \omega} \text{tr} [v_{s,x}^z G^r(\mathbf{k}, \omega) v_y G^a(\mathbf{k}, \omega)], \quad (14)$$

$$\sigma_{xy}^{z,\text{aa}} = \frac{e\hbar}{2} \sum_{\mathbf{k}, \omega} f(\omega) \text{tr} \left[v_{s,x}^z \left(\frac{\partial G^a(\mathbf{k}, \omega)}{\partial \omega} v_y G^a(\mathbf{k}, \omega) - G^a(\mathbf{k}, \omega) v_y \frac{\partial G^a(\mathbf{k}, \omega)}{\partial \omega} \right) - \text{h.c.} \right], \quad (15)$$

where f is the Fermi distribution function, $G^r(\mathbf{k}, \omega) = [\hbar\omega - \mathcal{H} + i\epsilon]^{-1}$ and $G^a(\mathbf{k}, \omega) = [G^r(\mathbf{k}, \omega)]^\dagger$ denote the retarded and the advanced Green's functions, respectively. These SHCs are analytically calculated in the clean limit (i.e., $\epsilon \rightarrow 0_+$) as shown in the Appendix A. Then, it becomes

$$\sigma_{xy}^z = e\hbar \sum_{\mathbf{k}} [f(E) - f(-E)] \Omega_{xy}^z, \quad (16)$$

where $f(E) = [1 + \exp[(E - \mu)/(k_B T)]]^{-1}$ denotes the Fermi distribution function and Ω_{xy}^z represents the spin Berry curvature; E , μ , k_B , and T represent the eigenvalue, chemical potential, Boltzmann's constant, and temperature, respectively. The spin Berry curvature Ω_{xy}^z can be obtained by calculating $\text{Tr}[\dots]$ in Eqs. (14) and (15). The spin Berry curvature Ω_{xy}^z is given by

$$\begin{aligned} \Omega_{xy}^z &= \sum_{E_n > E_{m \neq n}} i \frac{\langle n | v_{s,x}^z | m \rangle \langle m | v_y | n \rangle - (x \leftrightarrow y)}{[E_n(\mathbf{k}) - E_m(\mathbf{k})]^2} \\ &= \frac{\eta^2}{2\hbar E^3} \left[(M - t_z \cos k_z) \cos k_x \cos k_y \right. \\ &\quad \left. - t_{xy} (\cos k_x + \cos k_y) \right], \end{aligned} \quad (17)$$

where $|n\rangle$ denotes the wave function for $E_n (= E = \sqrt{a_1^2 + a_2^2 + a_3^2 + a_4^2 + a_5^2})$ of the n -th band for the Hamiltonian $H(\mathbf{k})$ in Eq. (1). It must be noted that, at $\beta = \gamma = 0$, the 4×4 model Hamiltonian can be decomposed into a 2×2 block diagonal in the spin \uparrow and \downarrow sectors, and the Berry curvatures for the \uparrow and \downarrow sectors Ω_{xy}^\uparrow and Ω_{xy}^\downarrow are defined, respectively. Then, we found that $\Omega_{xy}^z = \Omega_{xy}^\uparrow - \Omega_{xy}^\downarrow$, because the spin is conserved at $\beta = \gamma = 0$.

B. Low-energy description near Dirac points

Next, we analytically obtain the SHC in the low-energy effective Hamiltonian near DPs. Here we assume that DPs are located near the Γ point. The Hamiltonian is given by replacing $\sin k_i \rightarrow k_i + o(k_i^3)$ and $\cos k_i \rightarrow 1 - \frac{1}{2}k_i^2 + o(k_i^3)$ in Eq. (1) as follows^{7,13,14}:

$$\mathcal{H}(\mathbf{k}) = \hbar v (k_x s^z \sigma^x - k_y s^0 \sigma^y) + m(\mathbf{k}) s^0 \sigma^z, \quad (19)$$

where $v = \eta a / \hbar$ and a represent the velocity and the lattice constant, respectively. Here, $m(\mathbf{k})$ is a parameter that represents the band inversion and is given by⁷

$$m(\mathbf{k}) = -m_0 + m_1 k_z^2 + m_2 (k_x^2 + k_y^2) \quad (20)$$

with $m_0 = 2t_{xy} + t_z - M$, $m_1 = t_z a^2 / 2$, and $m_2 = t_{xy} a^2 / 2$. Here $m_1 m_0 > 0$ is required to obtain DPs. Below, we simply set the lattice constant $a = 1$.

Using Eqs. (19)-(20), we find that DPs are located at $\mathbf{k}_\pm = \pm(0, 0, k_0)$ with $k_0 \equiv \sqrt{m_0/m_1}$. Then, the

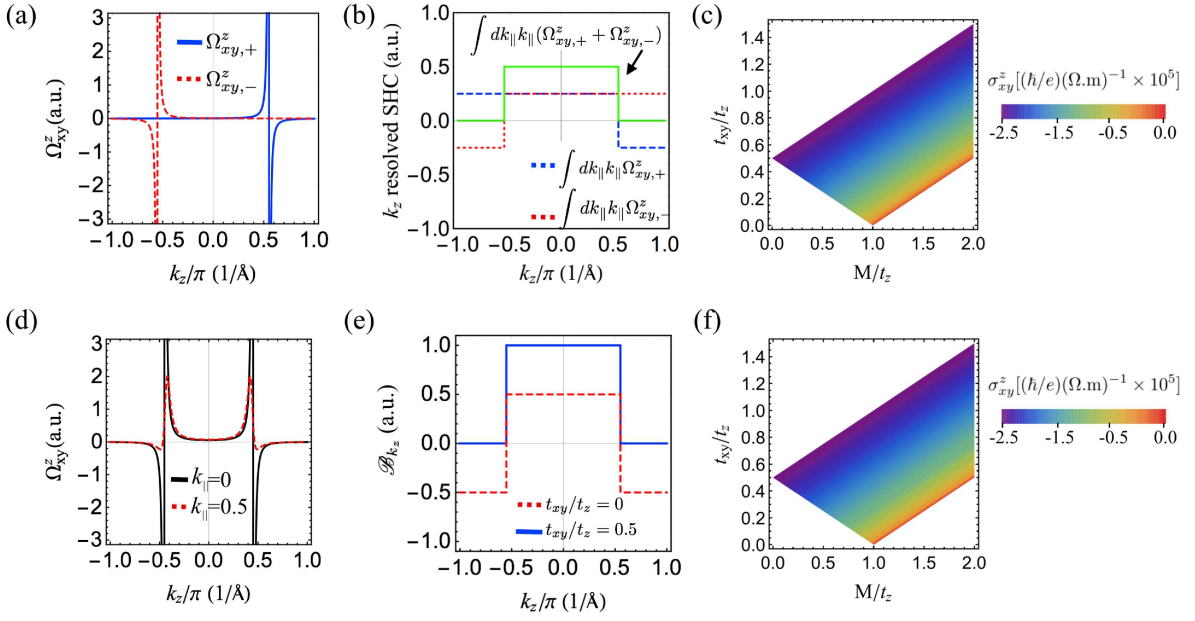


FIG. 2. (Color online) Spin Berry curvature and SHC in the low-energy description: (a) Momentum dependence of the spin Berry curvature near DPs, (b) k_z resolved SHC [$\int dk_{\parallel} k_{\parallel} \hbar (\Omega_{xy,+}^z + \Omega_{xy,-}^z)$], and (c) SHC in the TDSM phases in the low-energy description near the DPs, with $k_{\parallel} = \sqrt{k_x^2 + k_y^2}$. (d) Momentum dependence of the spin Berry curvature near the Γ point, (e) k_z resolved SHC \mathcal{B}_{k_z} , and (f) SHC in TDSM phases in the low-energy description near the Γ point. It is noticed that, at the $t_{xy} \rightarrow 0$ ($m_2 \rightarrow 0$) limit in (f), SHC becomes infinity. This result implies that the low-energy description does not work when $m_2 = 0$. Here, we used the parameters $\eta = 0.89$ eV, $t_z/\eta = -3.4$, and $t_{xy}/t_z = M/t_z = 0.5$, $a \approx 1\text{\AA}$, and the conductance quantum $2e^2/h = 7.75 \times 10^{-5} \Omega^{-1}$. The corresponding plot at that point ($t_{xy} \rightarrow 0$) was excluded because the magnitude of SHC diverges at $t_{xy} = 0$ ($m_2 = 0$).

Hamiltonian of Eq. (19) is linearized by expanding near the DPs \mathbf{k}_{\pm} , and the linearized Hamiltonian of each DP H_{\pm} is given by

$$H_{\pm} = \hbar v(k_x s^x - k_y s^y) \pm \hbar \tilde{v}(k_z \mp k_0) s^z \sigma^z \quad (21)$$

with $\tilde{v} = 2m_1 k_0/\hbar = \text{sgn}(m_1) 2\sqrt{m_0 m_1}/\hbar$. Using the Hamiltonian H_{\pm} , the SHC is given by,

$$\sigma_{xy}^z = \sigma_{xy,+}^z + \sigma_{xy,-}^z, \quad (22)$$

where $\sigma_{xy,\pm}^z$ is the SHC for the Hamiltonian H_{\pm} . This is a linearized model Hamiltonian near the DPs along the Γ -Z direction. Here, $\sigma_{xy,\pm}^z$ can be individually calculated based on the assumption of no interband interaction (no mixing effect) between each H_{\pm} . This SHC $\sigma_{xy,\pm}^z$ in the clean limit is obtained by a similar calculation as that in Eqs. (16)-(17) as follows:

$$\sigma_{xy,\pm}^z = e\hbar \sum_{\mathbf{k}} [f(E_{\pm}) - f(-E_{\pm})] \Omega_{xy,\pm}^z, \quad (23)$$

where $E_{\pm} = \hbar \sqrt{v^2(k_x^2 + k_y^2) + \tilde{v}^2(k_z \mp k_0)^2}$ and $\Omega_{xy,\pm}^z = \pm \hbar v^2 \tilde{v}(k_z \mp k_0)/(2E_{\pm}^3)$ [as shown in Fig. 2(a)] denote the eigenvalue and the spin Berry curvature for H_{\pm} , respectively. We perform the summation in Eq. (23) in a rotational symmetric manner along the k_z -axis. Because the system is a 2D spin Hall insulator for a fixed value of

k_z (except for $k_z = \pm k_0$), the 2D SHC is quantized to $(e^2/h) \times \mathbb{Z}$. As a result, the SHC in the overall system is given as follows (Appendix B):

$$\begin{aligned} \sigma_{xy}^z &= -e\hbar \int \frac{d^3 k}{(2\pi)^3} (\Omega_{xy,+}^z + \Omega_{xy,-}^z), \\ &= -\frac{e\hbar}{4\pi^2} \int_{-\infty}^{\infty} dk_z \int_0^{\infty} dk_{\parallel} k_{\parallel} (\Omega_{xy,+}^z + \Omega_{xy,-}^z) \\ &= -\frac{e}{8\pi^2} \int_{-\infty}^{\infty} dk_z \left[\text{sgn}[\tilde{v}(k_z - k_0)] - \text{sgn}[\tilde{v}(k_z + k_0)] \right] \end{aligned} \quad (24)$$

$$= \text{sgn}(m_1) \left(\frac{\hbar}{e} \right) \frac{e^2}{h} \frac{k_0}{\pi} \quad (25)$$

with $k_{\parallel} = \sqrt{k_x^2 + k_y^2}$. Thus, the above value is proportional to the distance between the DPs. This is similar to the anomalous Hall conductivity in Weyl semimetals, where the anomalous Hall conductivity depends only on the distance between Weyl points¹⁶.

From Eq. (24), the k_z resolved SHC (2D SHC) $\int dk_{\parallel} k_{\parallel} (\Omega_{xy,+}^z + \Omega_{xy,-}^z)$ takes a nonzero value only between the band crossing points $k_z \in [-k_0, k_0]$ [see Fig. 2(b)]. Therefore, the total SHC, which is obtained by k_z integral of the nonzero k_z resolved SHC, is proportional to the distance between the DPs [Fig. 2(c)]. Later, we confirm that this feature holds even beyond the low-

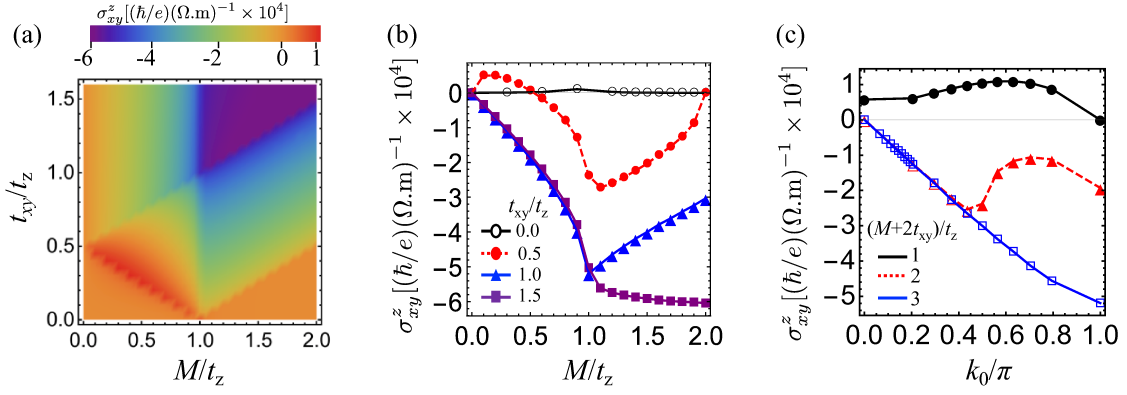


FIG. 3. (Color online) (a) Color density plot of the SHC for t_{xy}/t_z and M/t_z in the lattice model. (b) M/t_z dependence of SHC for several t_{xy}/t_z . (c) k_0 dependence of SHC for several $(M + 2t_{xy})/t_z$, which is parallel to the boundary line between TDSM and DSM phases. Here, $2k_0 = 2 \arccos(M - 2t_{xy})/t_z$ is the distance between the Dirac points along the Γ -X direction. Open and closed symbols represent $M/t_z > 1$ and $M/t_z < 1$, respectively. Here, we used the parameters $\eta = 0.89$ eV, $t_z/\eta = -3.4$, $\beta/t_z = 2\gamma/t_z = 0.67$, $a \sim 1\text{\AA}$, and $\mu = T = 0$.

energy description by performing the full lattice calculation of the SHC.

C. Mixing effects in low-energy description

In the previous subsection, we use the linearized Hamiltonian in Eq.(21) to evaluate the SHC. Here, we use the non-linearized version in Eq.(19), where the mixing between DPs is taken into account. The SHC is given by Eqs. (16)-(17) as follows:

$$\sigma_{xy}^z = e\hbar \sum_{\mathbf{k}} [f(\mathcal{E}) - f(-\mathcal{E})] \Omega_{xy}^z, \quad (26)$$

where $\mathcal{E} = \sqrt{\hbar^2 v^2 (k_x^2 + k_y^2) + m^2}$ and Ω_{xy}^z denote the energy dispersion and the spin Berry curvature for the Hamiltonian \mathcal{H} of Eq. (19), respectively. Here, the spin Berry curvature Ω_{xy}^z is similar to that in the linearized model [Fig.2(d)], where it diverges at the DPs. If \mathbf{k} integral is performed in a rotation symmetric manner as before, the SHC at the low-temperature limit is given by

$$\sigma_{xy}^z = -\left(\frac{\hbar}{e}\right) \times \frac{e^2}{h} \int_{-\infty}^{\infty} \frac{dk_z}{2\pi} \mathcal{B}_{k_z}, \quad (27)$$

$$\mathcal{B}_{k_z} \equiv \int_0^{\infty} dk_{\parallel} k_{\parallel} \hbar \Omega_{xy}^z(k_{\parallel}, k_z), \quad (28)$$

where \mathcal{B}_{k_z} is a non-dimensional value that denotes the 2D SHC of each k_z or the k_z resolved SHC.

First, we estimate \mathcal{B}_{k_z} in the limit $m_2 \rightarrow 0$ ($t_{xy} \rightarrow 0$). Then, it can be easily computed as follows (Appendix C):

$$\mathcal{B}_{k_z}(m_2 \rightarrow 0) = \frac{1}{2} \text{sgn}[-m_0 + m_1 k_z^2]. \quad (29)$$

Thus, SHC becomes infinity

$$\sigma_{xy}^z = -\text{sgn}(m_1) \times \infty, \quad (30)$$

which can be attributed to the fact that $\mathcal{B}_{k_z}(m_2 \rightarrow 0)$ stays nonzero for large $|k_z|$ [Fig. 2(e)]. This result implies that the low-energy description does not work when $m_2 \rightarrow 0$.

On the contrary, \mathcal{B}_{k_z} in $m_2 \neq 0$ (or $t_{xy} \neq 0$) becomes an integer

$$\mathcal{B}_{k_z} = \frac{1}{2} [\text{sgn}(-m_0 + m_1 k_z^2) - \text{sgn}(m_2)] \quad (31)$$

Here, \mathcal{B}_{k_z} depends on sign of parameters. Namely, if $m_0 < 0$, $m_1 < 0$, $m_2 < 0$ (e.g., parameters in Fig. 1), we have nonzero \mathcal{B}_{k_z} only for $k_z \in (-k_0, k_0)$, where $2k_0 = 2\sqrt{|m_0/m_1|}$ is the distance between the DPs. As a result, the k_z summation of \mathcal{B}_{k_z} , i.e., the total SHC converges [c.f., Fig. 2(e)], unlike that at $m_2 \rightarrow 0$. The obtained SHC is proportional to the distance between DPs.

We find that the SHC of the non-linearized model is the same as that of the linearized one, except when $m_2 = 0$. See Figs. 2(c) and (f). This is because the low-energy limit of the Hamiltonian in Eq.(1) preserves the spin in the z -direction since the spin-orbital coupling terms $a_4(\mathbf{k})$ and $a_5(\mathbf{k})$ are neglected. As a result, the SHC for each k_z is quantized, and thus the mixing between DPs does not affect the SHC.

D. Full lattice description

In this section, we show the SHC in the full lattice Hamiltonian. Using Eq. (16), we numerically compute $\sigma_{xy}^z(\mu = 0)$ at $T = 0$. The SHC depends on t_{xy}/t_z and M/t_z , as shown in Fig. 3. The color density plot of the SHC shows several blocks, which exactly correspond to different phases in the phase diagram of Fig. 1: in both DSM and normal insulator phases, the SHC is approximately zero. A nonzero SHC is obtained in the TDSM phase and the WTI/TCI phase. The phase dependence

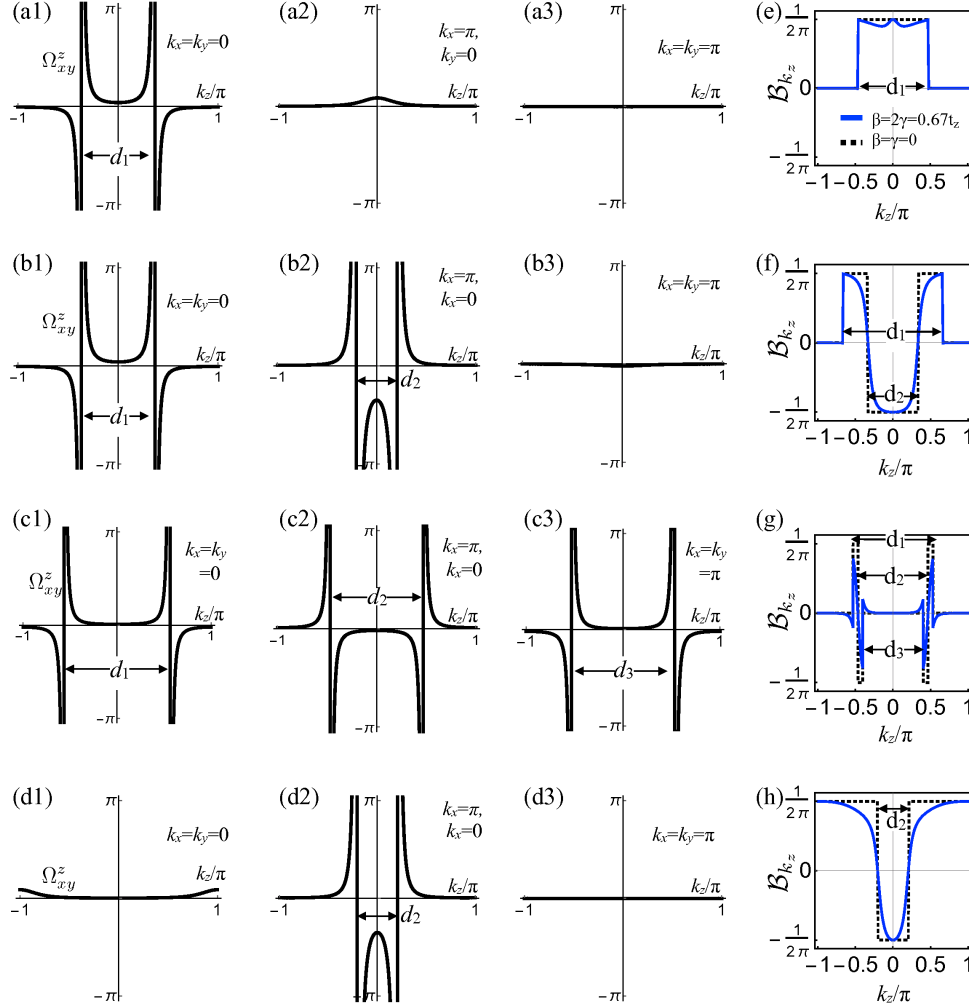


FIG. 4. Illustration of the k_z dependence of the spin Berry curvature $\Omega_{xy}^z(\mathbf{k})$ at the Γ , X , and M points in the Brillouin zone in (a1)-(a3) TDSM phase with $M/t_z \geq 1$, (b1)-(b3) TDSM with $M/t_z < 1$, (c1)-(c3) DSM, and (d1)-(d3) WTI/TCI phase with $M/t_z \leq 1$ at $\beta = \gamma = 0$. Here, d_1 , d_2 , and d_3 denote the distance between the Dirac points along the k_z axis at the Γ , X , and M points, respectively. (e)-(h) 2D integral of the spin Berry curvature in each phase without (dotted lines) and with SOC (blue lines).

of the SHC is one of the main results in this paper. We also confirm that the SHC shows qualitatively the same behaviors even at $T = 300$ K.

The SHC changes drastically at the line $M/t_z = 1$ [see also Fig. 3(b)]. In particular, the SHC depends in a different manner on the distance between DPs. Figure 3(c) depicts how the SHC depends on the distance between DPs for several $(M + 2t_{xy})/t_z$. Here, $2k_0 [= \arccos(M - 2t_{xy})/t_z]$ is the distance between the DPs along the Γ - X direction, and the open and closed symbols in Fig. 3(b) denote the data for $M/t_z < 1$ and $M/t_z > 1$, respectively. In contrast to the low-energy description in Secs. III B and III C, we find that the SHC is proportional to k_0 only when $M/t_z > 1$.

This phase dependence of the SHC can be explained

by the 2D integral of the spin Berry curvature

$$\mathcal{B}_{k_z} \equiv \hbar \sum_{k_x, k_y} \Omega_{xy}^z(\mathbf{k}) \quad (32)$$

in each phase. First, we consider \mathcal{B}_{k_z} at $\beta = \gamma = 0$, where the spin in the z -direction is preserved. Because the spin Berry curvature Ω_{xy}^z is inversely proportional to the cube of the energy dispersion E^3 , it strongly depends on the location of the DPs of each phase. For example, when the DPs are located only at the Γ point in the TDSM phases with $M/t_z > 1$, the spin Berry curvature diverges only at the DPs along the Γ - X direction [see Fig. 4(a1)-(a3)]. Furthermore, its divergence is separated by d_1 , where $d_1 \equiv 2 \arccos(M - 2t_{xy})/t_z$ is the distance between DPs along the Γ - X direction. Then, the non-dimensional parameter \mathcal{B}_{k_z} is obtained from the distance

as $\mathcal{B}_{k_z} = \frac{1}{2\pi} \text{sgn}(d_1 - |k_z|)$ [see Fig. 4(e)]. Therefore, the SHC is proportional to d_1 from Eq. (16) [c.f. Fig. 3(b)].

On the contrary, the TDSM phase with $M/t_z < 1$ hosts gapless DPs not only along the Γ -Z line but also along the X -R line. As a result, the 2D integral of the spin Berry curvature \mathcal{B}_{k_z} is described by d_1 and d_2 as $\frac{1}{2\pi} [\text{sgn}(d_1 - |k_z|) - 2\text{sgn}(d_2 - |k_z|)]$, where $d_2 = 2 \arccos(M/t_z)$ is the distance between DPs along the X -A direction. [Fig. 4(b1)-(b3)]. The SHC depends on both d_1 and d_2 , as shown in Fig. 4(f). Thus, even in the same TDSM phase, the SHC for $M/t_z < 1$ shows different behaviors than that for $M/t_z > 1$. (See also Sec.IV.)

Similarly, because the DSM phase possesses gapless DPs on the Γ -Z, X -R, and M -A lines, the spin Berry curvature Ω_{xy}^z diverges at those points [Fig. 4(c1)-(c3)]. As a result, \mathcal{B}_{k_z} depends on d_1 , d_2 , and d_3 as follows: $\mathcal{B}_{k_z} = \frac{1}{2\pi} [\text{sgn}(d_1 - |k_z|) - 2\text{sgn}(d_2 - |k_z|) + \text{sgn}(d_3 - |k_z|)]$, where d_3 is the distance between the DPs along the M -A direction. Because the three terms in \mathcal{B}_{k_z} are cancelled for a finite region of k_z , the SHC is strongly suppressed in the DSM phase. For $\beta = \gamma = 0$, we also find that the WTI/TCI phase with $M/t_z < 1$ has gapless DPs along X -R line, and thus the SHC in the WTI/TCI phase in $M/t_z < 1$ and $M/t_z > 1$ regimes are quantized to $e^2/h \times [1 - d_2/(2\pi)]$ and e^2/h , respectively.

In the presence of the spin-orbital coupling (SOC) with nonzero β and γ , the DPs along the X -R line in $M/t_z < 1$ show a narrow gap. Whereas the spin Berry curvature at the narrow gap [Fig. 4(b2) and (c2)] does not diverge, it contributes to the 2D integral of the SHC, similar to that in $\beta = \gamma = 0$ [Fig. 4(f)-(h)]. Thus, even for nonzero β and γ , the magnitude of SHC could be qualitatively explained by the location of the DPs and the distance between DPs. On the other hand, $\mathcal{B}_{k_z \neq 0, \pi}$ is not quantized to $1/(2\pi)$ in the presence of SOC [compare Fig. 4(f) and (g)] since the spin in the z -direction is no longer conserved. (We note that $\mathcal{B}_{k_z=0, \pi}$ is quantized because of the mirror reflection symmetry with respect to the z -axis.)

IV. DISCUSSION

First, we compare the low-energy description in Secs.III B-III C and the lattice description in Sec.III D. The SHC in the low-energy description is proportional to the distance between the DPs [Eq. (25)]. This result is consistent with that in the lattice description of the TDSM phase with $M/t_z > 1$; however, it does not agree with that with $M/t_z < 1$. This is because, in $M/t_z < 1$, DPs with a tiny gap appear along the X -R line, which provide additional contributions for the spin Berry curvature. Thus, the simple low-energy description given in Sec.III B is valid only in the TDSM phase with $M/t_z > 1$.

From the SHC of the lattice description, it is observed that the parameter dependence of SHC clearly changes at the line $M/t_z = 1$. The change can be explained by the mirror Chern numbers for the horizontal mirror reflection

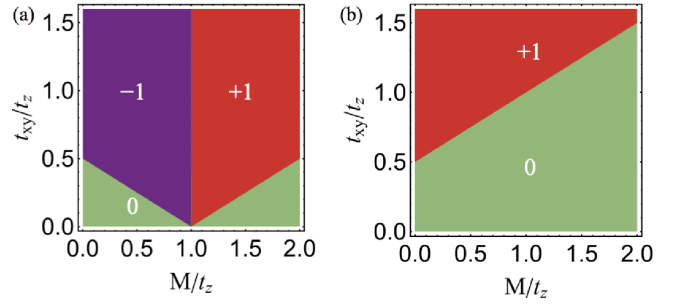


FIG. 5. Phase diagram of the mirror Chern number $n_{\mathcal{M}}$ for M/t_z and t_{xy}/t_z at (a) $k_z = 0$ and (b) $k_z = \pi$ planes.

symmetry. The mirror Chern numbers are defined as,

$$n_{\mathcal{M}}(k_z) \equiv \frac{1}{2} [n_{+i}(k_z) - n_{-i}(k_z)], \quad (33)$$

where $k_z = 0, \pi$ and $n_{\pm i}$ is the Chern number for mirror sub-sectors labeled with the mirror eigenvalues $\pm i$, which correspond to the spin-up and spin-down sectors. Figure 5 shows the mirror Chern numbers in our models, which indicates that $n_{\mathcal{M}}(k_z = 0)$ changes at the line $M/t_z = 1$. Corresponding to the nonzero mirror Chern numbers, we also have surface states. The surface states of each phase are summarized in Appendix D.

We note that the region in $M/t_z < 1$ and that $M/t_z > 1$ support strong and weak topological phases, respectively: For $M/t_z < 1$ ($M/t_z > 1$), $n_{\mathcal{M}}(k_z = 0)$ and $n_{\mathcal{M}}(k_z = \pi)$ are different (the same), which implies a strong (weak) mirror topological phase¹⁷. We also point out that a bulk topological index can be defined even in the presence of bulk gapless points¹⁸.

Next, we discuss the mechanism of SHC. Although we assume the clean limit and only consider intrinsic SHC, the actual system may have the extrinsic SHC due to disorders. According to Ref. 19, the intrinsic SHC dominates when the longitudinal conductivity σ_{xx} is in the range $10^4(\Omega \cdot \text{cm})^{-1} < \sigma_{xx} < 10^6(\Omega \cdot \text{cm})^{-1}$. For Cd_3As_2 , A4 and A6 samples in Ref.3 satisfy this condition, which suggests that the intrinsic SHC is dominant. Since the band structure of Cd_3As_2 ²⁰ is consistent with that in the TDSM phase with $M/t_z > 1$, our result estimates that Cd_3As_2 shows $\sigma_{xy}^z \sim 10^4(\hbar/e) \times (\Omega \cdot \text{m})^{-1}$. The estimated value is comparable to the huge SHC in heavy metals⁹.

Finally, we point out that the SHC could identify phases in the phase diagram of Fig. 3. The SHC in the TDSM and WTI/TCI phases with $M/t_z > 1$ is large and negative, while that in DSM phase is small and negative. Therefore, transport measurements of the spin Hall effect can distinguish these topological phases.

V. CONCLUSION

We theoretically studied the SHC in an effective model Hamiltonian of TDSM in the low-energy and the lattice

descriptions. We found that the SHC in the linearized low-energy description is a qualitatively good approximation for the SHC in the lattice description only in the TDSM phase with $M/t_z > 1$ (i.e., the DPs are located only along the Γ -Z direction). In addition, we found that the SHC behaves differently [for some parameters] depending on the phase in the lattice description. It can be explained by the 2D SHC of each k_z and by the location of the DPs. The phase dependence of the SHC obtained in this study can be applied in determining whether a material is in the DSM or the TDSM phase by transport

measurement of the spin Hall effect.

ACKNOWLEDGMENTS

The authors thank S. Kobayashi for helpful discussion. This work was supported by Grant-in-Aid for Scientific Research(B) 17H02922, Early-Career Scientists 19K14658, the Grants-in-Aid for Scientific Research on Innovative Areas “Topological Material Science”, JSPS (Grant Nos. JP15H05855, JP15K21717, JP15H05853), and JST CREST (No: JPMJCR19T2), Japan. This project was supported in part by JSPS and ISF under Japan-Israel Cooperative Program.

-
- ¹ B.-J. Yang and N. Nagaosa, Nat. Comm. **5**, 4898 (2014).
 - ² Z. K. Liu, J. Jiang, B. Zhou, Z. J. Wang, Y. Zhang, H. M. Weng, D. Prabhakaran, S.-K. Mo, H. Peng, P. Dudin, T. Kim, M. Hoesch, Z. Fang, X. Dai, Z. X. Shen, D. L. Feng, Z. Hussain, and Y. L. Chen, Nat. Mater. **13**, 677 (2014).
 - ³ T. Liang, Q. Gibson, M. N. Ali, M. Liu, R. J. Cava, and N. P. Ong, Nat Mater **14**, 280 (2014).
 - ⁴ L. P. He, X. C. Hong, J. K. Dong, J. Pan, Z. Zhang, J. Zhang, and S. Y. Li, Phys. Rev. Lett. **113**, 246402 (2014).
 - ⁵ M. N. Ali, Q. Gibson, S. Jeon, B. B. Zhou, A. Yazdani, and R. J. Cava, Ino. Chem. **53**, 4062 (2014).
 - ⁶ M. Uchida, Y. Nakazawa, S. Nishihaya, K. Akiba, M. Kriener, Y. Kozuka, A. Miyake, Y. Taguchi, M. Tokunaga, N. Nagaosa, Y. Tokura, and M. Kawasaki, Nat. Comm. **8**, 2274 (2017).
 - ⁷ A. A. Burkov and Y. B. Kim, Phys. Rev. Lett. **117**, 136602 (2016).
 - ⁸ Y. Araki, Sci. Rep. **8**, 15236 (2018).
 - ⁹ A. Hoffmann, IEEE Transactions on Magnetism **49**, 5172 (2013).
 - ¹⁰ J. Sinova, S. O. Valenzuela, J. Wunderlich, C. H. Back, and T. Jungwirth, Rev. Mod. Phys. **87**, 1213 (2015).
 - ¹¹ M. M. Vazifeh and M. Franz, Phys. Rev. Lett. **111**, 027201 (2013).
 - ¹² P. Goswami and S. Tewari, Phys. Rev. B **88**, 245107 (2013).
 - ¹³ S. Kobayashi and M. Sato, Phys. Rev. Lett. **115**, 187001 (2015).
 - ¹⁴ T. Hashimoto, S. Kobayashi, Y. Tanaka, and M. Sato, Phys. Rev. B **94**, 014510 (2016).
 - ¹⁵ T. Tanaka, H. Kontani, M. Naito, T. Naito, D. S. Hirashima, K. Yamada, and J. Inoue, Phys. Rev. B **77**, 165117 (2008).
 - ¹⁶ N. P. Armitage, E. J. Mele, and A. Vishwanath, Rev. Mod. Phys. **90**, 015001 (2018).
 - ¹⁷ C.-K. Chiu, H. Yao, and S. Ryu, Phys. Rev. B **88**, 075142 (2013).
 - ¹⁸ M. Sato and S. Fujimoto, Phys. Rev. Lett. **105**, 217001 (2010).
 - ¹⁹ N. Nagaosa, J. Sinova, S. Onoda, A. H. MacDonald, and N. P. Ong, Rev. Mod. Phys. **82**, 1539 (2010).
 - ²⁰ Z. Wang, H. Weng, Q. Wu, X. Dai, and Z. Fang, Phys. Rev. B **88**, 125427 (2013).
 - ²¹ P. Streda, Journal of Physics C: Solid State Physics **15**, L717 (1982).

Appendix A: Derivation of SHC

In this section, we derive the SHC using Green's functions. Here, the Green's function is described as,

$$G^a(\mathbf{k}, \omega) = \frac{\mathcal{P}_+(\mathbf{k})}{\hbar\omega - i\delta - E(\mathbf{k})} + \frac{\mathcal{P}_-(\mathbf{k})}{\hbar\omega - i\delta + E(\mathbf{k})} \quad (\text{A1})$$

Using Eq. (A1), we have

$$\begin{aligned} \sigma_{xy}^{z,\text{ra}} + \sigma_{xy}^{z,\text{aa}} &= e\hbar \sum_{\mathbf{k}, \omega} \left\{ \frac{\partial f_\omega}{\partial \omega} \text{tr} [v_{s,x}^z G_{\mathbf{k}, \omega}^r v_y G_{\mathbf{k}, \omega}^a] + \frac{1}{2} \text{tr} \left[v_{s,x}^z \left(\frac{\partial G^a}{\partial \omega} v_y G^a - G^a v_y \frac{\partial G^a}{\partial \omega} \right) - \text{h.c.} \right] \right\} \\ &= e\hbar^2 \sum_{\mathbf{k}, \omega} \left\{ \frac{\partial f_\omega}{\partial (\hbar\omega)} \text{tr} \left[\frac{v_{s,x}^z \mathcal{P}_+ v_y \mathcal{P}_+}{|h - E|^2} + \frac{v_{s,x}^z \mathcal{P}_- v_y \mathcal{P}_-}{|h + E|^2} + \frac{v_{s,x}^z \mathcal{P}_+ v_y \mathcal{P}_-}{(h^* - E)(h + E)} + \frac{v_{s,x}^z \mathcal{P}_- v_y \mathcal{P}_+}{(h - E)(h^* + E)} \right] \right. \\ &\quad \left. + \text{tr} [v_{s,x}^z (\mathcal{P}_+ v_y \mathcal{P}_- - \mathcal{P}_- v_y \mathcal{P}_+)] \left[\frac{f_\omega E}{[h^2 - E^2]^2} - \text{h.c.} \right] \right\}, \end{aligned} \quad (\text{A2})$$

where we used $h \equiv \hbar\omega - i\delta$, and

$$\text{tr} [v_{s,x}^z G_{\mathbf{k}, \omega}^r v_y G_{\mathbf{k}, \omega}^a] = \text{tr} \left[\frac{v_{s,x}^z \mathcal{P}_+ v_y \mathcal{P}_+}{|h - E|^2} + \frac{v_{s,x}^z \mathcal{P}_- v_y \mathcal{P}_-}{|h + E|^2} + \frac{v_{s,x}^z \mathcal{P}_+ v_y \mathcal{P}_-}{(h^* - E)(h + E)} + \frac{v_{s,x}^z \mathcal{P}_- v_y \mathcal{P}_+}{(h - E)(h^* + E)} \right] \quad (\text{A3})$$

$$\frac{\partial G^a(\mathbf{k}, \omega)}{\partial \omega} = -\hbar \left[\frac{\mathcal{P}_+(\mathbf{k})}{[h - E(\mathbf{k})]^2} + \frac{\mathcal{P}_-(\mathbf{k})}{[h + E(\mathbf{k})]^2} \right] \quad (\text{A4})$$

Here, $\text{tr} [v_{s,x}^z \mathcal{P}_\pm v_y \mathcal{P}_\pm]$ and $\text{tr} [v_{s,x}^z \mathcal{P}_\pm v_y \mathcal{P}_\mp]$ in Eq. (A2) are estimated from

$$\text{tr} [v_{s,x}^z v_y] = 0 \quad (\text{A5})$$

$$\text{tr} [v_{s,x}^z \mathcal{H} v_y \mathcal{H}] = 0 \quad (\text{A6})$$

$$\text{tr} [\mathcal{H} (v_{s,x}^z v_y + v_y v_{s,x}^z)] = 0 \quad (\text{A7})$$

and

$$\text{tr} [v_{s,x}^z \mathcal{P}_\pm v_y \mathcal{P}_\pm] = \frac{1}{4} \text{tr} \left[v_{s,x}^z v_y + v_{s,x}^z \mathcal{H} v_y \mathcal{H} \pm \frac{1}{E} \mathcal{H} (v_{s,x}^z v_y + v_y v_{s,x}^z) \right] = 0, \quad (\text{A8})$$

$$\text{tr} [v_{s,x}^z \mathcal{P}_\pm v_y \mathcal{P}_\mp] = \frac{1}{4} \text{tr} \left[v_{s,x}^z v_y - v_{s,x}^z \mathcal{H} v_y \mathcal{H} \pm \frac{1}{E} \mathcal{H} (v_{s,x}^z v_y - v_y v_{s,x}^z) \right] = \pm \frac{1}{4E} \text{tr} [\mathcal{H} (v_{s,x}^z v_y - v_y v_{s,x}^z)]. \quad (\text{A9})$$

Here, Eq. (A9) is also represented by the spin Berry curvature $\Omega_{xy}^z(\mathbf{k})$:

$$\text{tr} [v_{s,x}^z \mathcal{P}_\pm v_y \mathcal{P}_\mp] = \pm 2i \Omega_{xy}^z(\mathbf{k}) E^2(\mathbf{k}). \quad (\text{A10})$$

Here, the spin Berry curvature is defined by

$$\begin{aligned} \Omega_{xy}^z &\equiv \sum_{m \neq n, E_n > E_m} i \frac{\langle n, \mathbf{k} | v_{s,x}^z | m, \mathbf{k} \rangle \langle m, \mathbf{k} | v_y | n, \mathbf{k} \rangle - (x \leftrightarrow y)}{[E_n(\mathbf{k}) - E_m(\mathbf{k})]^2} \\ &= \frac{\eta^2}{2\hbar E^3} \left[\cos k_x \cos k_y (M - t_z \cos k_z) - t_{xy} (\cos k_x + \cos k_y) \right], \end{aligned} \quad (\text{A11})$$

where $|m, \mathbf{k}\rangle$ denotes the wave function for E_m of the m -th band. The spin Berry curvature is given by $\text{tr} [v_{s,x}^z \mathcal{P}_\pm v_y \mathcal{P}_\mp]$. As a result, we have,

$$\sigma_{xy}^{z,\text{ra}} + \sigma_{xy}^{z,\text{aa}} = e\hbar^2 \sum_{\mathbf{k}, \omega} [2iE^2 \Omega_{xy}^z(\mathbf{k})] \left\{ \frac{\partial f_\omega}{\partial (\hbar\omega)} \left[\frac{1}{(h^* - E)(h + E)} - \text{h.c.} \right] + 2 \left[\frac{f_\omega E}{[h^2 - E^2]^2} - \text{h.c.} \right] \right\}. \quad (\text{A12})$$

where $\mathcal{P}_\pm(\mathbf{k}) = [1 \pm \mathcal{H}/E(\mathbf{k})]/2$ denotes the projected operator, and $\delta > 0$ is an infinitesimal value. The first and the second terms of the above equation imply the contribution from the dispersions of $E(\mathbf{k})$ and $-E(\mathbf{k})$, respectively.

Here, the ω integral in the above equation is obtained as follows:

$$\begin{aligned}
& \sum_{\omega} \left\{ \frac{\partial f_{\omega}}{\partial(\hbar\omega)} \left[\frac{1}{(\hbar^* - E)(\hbar + E)} - \text{h.c.} \right] + 2 \left[\frac{f_{\omega} E}{[(\hbar\omega - i\delta)^2 - E^2]^2} - \text{h.c.} \right] \right\} \\
&= \frac{1}{2\pi\hbar} \int_{-\infty}^{\infty} d\hbar\omega \left[\frac{\partial f_{\omega}}{\partial(\hbar\omega)} \left[\frac{1}{(\hbar\omega + i\delta - E)(\hbar\omega - i\delta + E)} - \text{h.c.} \right] + 2 \left[\frac{f_{\omega} E}{[(\hbar\omega - i\delta) - E]^2 [(\hbar\omega - i\delta) + E]^2} - \text{h.c.} \right] \right\} \\
&= \frac{1}{2\pi\hbar} \oint_{\text{upper half circle}} dz \left\{ f'_z \left[\frac{1}{[z - (E - i\delta)][z - (-E + i\delta)]} - \frac{1}{[z - (E + i\delta)][z - (-E - i\delta)]} \right] \right. \\
&\quad \left. + 2 \left[\frac{f_z E}{[z - (E + i\delta)]^2 [z - (-E + i\delta)]^2} - \frac{f_z E}{[z - (E - i\delta)]^2 [z - (-E - i\delta)]^2} \right] \right\} \\
&= \frac{i}{2\hbar} \left[\frac{f'_z(-E + i\delta)}{-E + i\delta} - \frac{f'_z(E + i\delta)}{E + i\delta} \right] + 2 \times \frac{i}{4\hbar} \left[\frac{f'(E) + f'(-E)}{E} - \frac{f(E) - f(-E)}{E^2} \right] \tag{A13}
\end{aligned}$$

$$=_{\delta \rightarrow 0} -\frac{i}{2\hbar} \frac{f'_z(E) + f'_z(-E)}{E} + 2 \times \frac{i}{4\hbar} \left[\frac{f'(E) + f'(-E)}{E} - \frac{f(E) - f(-E)}{E^2} \right] \tag{A14}$$

$$= -\frac{i}{2\hbar} \frac{f(E) - f(-E)}{E^2} \tag{A15}$$

As a result, we obtain

$$\sigma_{xy}^{z,\text{ra}} + \sigma_{xy}^{z,\text{aa}} = e\hbar \sum_{\mathbf{k}} [f(E) - f(-E)] \Omega_{xy}^z(\mathbf{k}). \tag{A16}$$

Here, the SHC associates the Fermi sea term, according to Streda formal^{15,21}.

Appendix B: Calculation of SHC in the low-energy description

Here, we show the SHC in the low-energy description. The SHC is obtained from the spin Berry curvature in the effective model Hamiltonian $\mathcal{H}(\mathbf{k})$ by replacing $\sin k_i \rightarrow k_i a + o(k_i^3)$, $\cos k_i \rightarrow 1 - \frac{1}{2} k_i^2 a^2 + o(k_i^3)$, and $\eta \rightarrow \hbar v$ in Eq. (2)-(4) as follows:

$$\Omega_{xy}^z(k_x, k_y, k_z) = \frac{\hbar v^2}{2} \frac{m(\mathbf{k})}{E^3}$$

where we used $\eta a = \hbar v$ and $m(\mathbf{k}) = -m_0 + m_1 k_z^2 + m_2(k_x^2 + k_y^2)$. Here, the spin Berry curvature $\Omega_{xy}^z(k_x, k_y, k_z)$ can be estimated near the Dirac points $\mathbf{k}_{\pm} = (0, 0, \pm k_0)$. Then, the spin Berry curvature linearized \mathbf{k} near the DPs $\Omega_{xy,\pm}^z$ is given by the energy dispersion $E_{\pm}(\mathbf{k} \sim \mathbf{k}_{\pm}) = \hbar \sqrt{v^2(k_x^2 + k_y^2) + \tilde{v}^2(k_z \mp k_0)^2}$ as follows:

$$\Omega_{xy,\pm}^z(\mathbf{k} \sim \mathbf{k}_{\pm}) = \pm \frac{\hbar v^2}{2} \frac{\hbar \tilde{v}(k_z \mp k_0)}{E_{\pm}^3} \tag{B1}$$

$$= \pm \frac{\hbar v^2}{2} \frac{\hbar \tilde{v}(k_z \mp k_0)}{[\hbar^2 v^2(k_x^2 + k_y^2) + \hbar^2 \tilde{v}^2(k_z \mp k_0)^2]^{3/2}} \tag{B2}$$

As a result, we obtain

$$\begin{aligned}
\sigma_{xy}^z &= -e\hbar \sum_{\pm} \int \frac{dk^3}{(2\pi)^3} \Omega_{xy,\pm}^z(k_x, k_y, k_z) \\
&= -\frac{e\hbar}{4\pi^2} \sum_{\pm} \int_{-\infty}^{\infty} dk_z \int_0^{\infty} dk_{\parallel} k_{\parallel} \Omega_{xy,\pm}^z(k_{\parallel}, k_z) \\
&= -\frac{e\hbar}{4\pi^2} \sum_{\pm} \int_{-\infty}^{\infty} dk_z \int_0^{\infty} dk_{\parallel} k_{\parallel} \left[\pm \frac{\hbar v^2}{2} \frac{\hbar \tilde{v}(k_z \mp k_0)}{[\hbar^2 v^2 k_{\parallel}^2 + \hbar^2 \tilde{v}^2 (k_z \mp k_0)^2]^{3/2}} \right] \\
&= -\frac{e}{8\pi^2} \sum_{\pm} \int_{-\infty}^{\infty} dk_z \int_0^{\infty} d\epsilon \left[\pm \frac{\hbar \tilde{v}(k_z \mp k_0) \epsilon}{[\epsilon^2 + \hbar^2 \tilde{v}^2 (k_z \mp k_0)^2]^{3/2}} \right] \\
&= -\frac{e}{8\pi^2} \int_{-\infty}^{\infty} dk_z \left[\text{sgn}[\tilde{v}(k_z - k_0)] - \text{sgn}[\tilde{v}(k_z + k_0)] \right] \tag{B3}
\end{aligned}$$

$$= \text{sgn}(\tilde{v}) \frac{ek_0}{2\pi^2} \tag{B4}$$

$$= \text{sgn}(m_1) \left(\frac{\hbar}{e} \right) \frac{e^2}{2\pi\hbar} \frac{k_0}{\pi}, \tag{B5}$$

where we used $\tilde{v} = \text{sgn}(m_1) 2\sqrt{m_0 m_1}/\hbar$.

Appendix C: Calculation of SHC in the low-energy description with the mixing effect

In this section, we calculate the SHC in the quadratic Hamiltonian. The SHC is given by Eq. (19) as

$$\sigma_{xy}^z = -\frac{e\hbar}{4\pi^2} \int_{-\infty}^{\infty} dk_z \int_0^{\infty} dk_{\parallel} k_{\parallel} \Omega_{xy}^z(k_{\parallel}, k_z) \tag{C1}$$

$$= -\left(\frac{\hbar}{e} \right) \times \frac{e^2}{h} \int_{-\infty}^{\infty} \frac{dk_z}{2\pi} \mathcal{B}_{k_z} \tag{C2}$$

with

$$\mathcal{B}_{k_z} \equiv \int_0^{\infty} dk_{\parallel} k_{\parallel} \hbar \Omega_{xy}^z(k_{\parallel}, k_z), \tag{C3}$$

$$\Omega_{xy}^z(\mathbf{k}) = \frac{\hbar v^2 - m_0 + m_1 k_z^2 - m_2 (k_x^2 + k_y^2)}{2 E^3} \tag{C4}$$

$$E(\mathbf{k}) = \sqrt{\hbar^2 v^2 (k_x^2 + k_y^2) + m^2(\mathbf{k})} \tag{C5}$$

$$m(\mathbf{k}) = -m_0 + m_1 k_z^2 + m_2 (k_x^2 + k_y^2) \tag{C6}$$

If $m_2 = 0$ (or $t_{xy} = 0$), because $m(\mathbf{k})$ is independent of k_x and k_y , σ_{xy}^z is easily calculated as follows:

$$\mathcal{B}_{k_z} = \frac{1}{2} \text{sgn}[-m_0 + m_1 k_z^2] \tag{C7}$$

$$\sigma_{xy}^z = -\left(\frac{\hbar}{e} \right) \times \frac{e^2}{h} \int_{-\infty}^{\infty} \frac{dk_z}{2\pi} \frac{1}{2} \text{sgn}[-m_0 + m_1 k_z^2] \rightarrow -\text{sgn}(m_1) \times \infty. \tag{C8}$$

Appendix D: Surface states

Because the nonzero mirror Chern number ensures surface states, we consider the surface states of each phase [k_x surface at $k_z = 0$ and $k_z = \pi$]. As a result, the surface states in WTI/TCI of $M/t_z < 1$ and $M/t_z > 1$ are different, as shown in Fig.6. It is further found that surface states exist in WTI/TCI and TDSM phases. In the WTI/TCI phase $M/t_z < 1$ ($M/t_z > 1$), the band crossing points of the surface states at $k_z = 0$ and $k_z = \pi$ are present at different

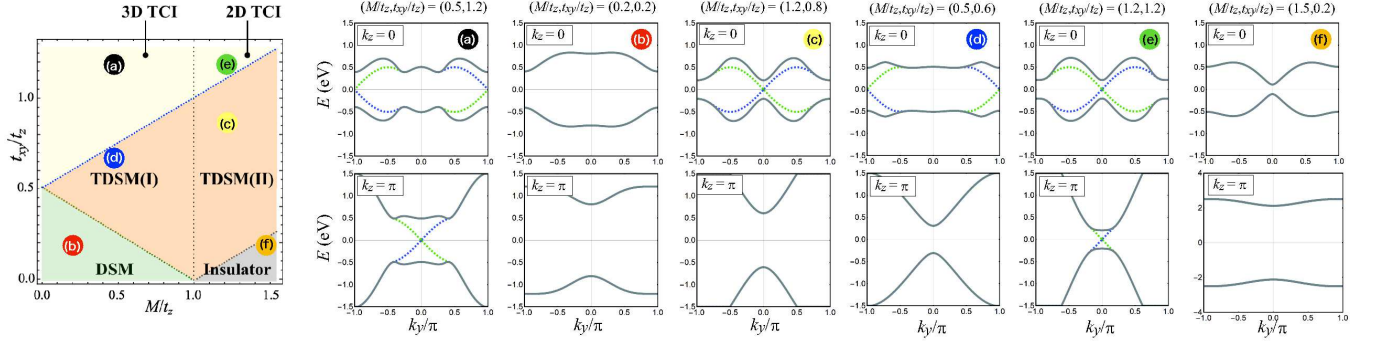


FIG. 6. (100) surface states at (upper panels) $k_z = 0$ and (lower panels) $k_z = \pi$ in WTI/TCI phase of (a) $M/t_z < 1$ and (b) $M/t_z > 1$, in TDSM phase of (c) $M/t_z < 1$ and (d) $M/t_z > 1$, and in (e) DSM phase. Blue and green dotted lines represent the surface states of up-spin and down-spin sectors, respectively. The left panel shows the phase diagram.

locations (at the same location $k_y = 0$). Furthermore, the band crossing points are located at symmetric positions, which could have been caused by mirror-reflection symmetry.